Global Kinetic Model of a Three-Way-Catalyst-Coated Gasoline Particulate Filter: Catalytic Effects of Soot Accumulation

N.B. When citing this work, cite the original published paper.

(article starts on next page)

Article

Global Kinetic Model of a Three-Way-Catalyst-Coated Gasoline Particulate Filter: Catalytic Effects of Soot Accumulation

Jesus De Abreu Goes, Louise Olsson,* and Timothy C. Watling

Read Online

ACCESS | 📊 Metrics & More | 📑 Article Recommendations | 📄 Supporting Information

Global Kinetic Model of a TWC-Coated GPF
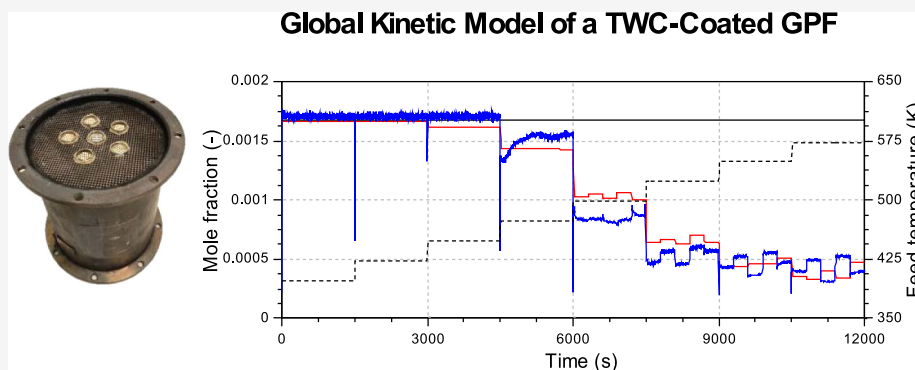
ABSTRACT: In the present study, a global kinetic model of three-way-catalyst-coated gasoline particulate filters was developed to understand the relevant kinetic mechanisms taking place both in clean and real soot-loaded filters. The model involves reaction rate expressions for CO, C_2H_4, and C_7H_8 conversion over a model $Pd/CeZr/Al_2O_3$ catalyst, hydrothermally treated at 650 °C. Particularly, a new rate expression was proposed for ethylene based on the distinctive experimental trends observed for this hydrocarbon. The model predicted satisfactorily the conversion of all three reductants under different experimental conditions. The soot inhibition effect was also modeled by the reduction of the number of active sites. Interestingly, ethylene was less affected compared to other reductants by the presence of soot due to the formation of less stable and more reactive species on the catalyst surface.

1. INTRODUCTION

The three-way catalyst (TWC) converter is a widely and successfully utilized component for the removal of carbon monoxide (CO), unburned hydrocarbon (HC), and nitrogen oxide (NO_x) pollutants of stoichiometric engines. As the emission limits are becoming more rigorous, the design and optimization of TWCs are being increasingly supported by mathematical modeling, reducing the amount of experimentation required. This approach particularly needs a detailed understanding of the relevant reaction mechanisms and kinetic processes taking place simultaneously and interactively over the whole range of operating conditions. Multiple models have appeared in the literature describing these mechanisms over TWC converters with varying degrees of complexity. For instance, Dubien et al.[1] developed kinetic expressions for fast- and slow-oxidizing hydrocarbons, inhibiting species and steam reforming reactions over TWC based on the widely used rate expressions proposed by Voltz et al.[2] and Subramanian and Varma.[3] Nibbelke et al.[4,5] developed a steady-state and transient microkinetic model for the CO oxidation over a $Pt/Rh/CeO_2/Al_2O_3$ catalyst formulation. More recently, Hauck et al.[6] simulated the CO oxidation over pretreated and aged Pd/Rh-based commercial TWC converters using a

microkinetic reaction model. Kang et al.[7] developed reaction kinetics for a Pd/Rh double-layered TWC by combining the activity function derived for the Pd-based and Rh-based catalysts. Kang et al.[8] also developed a model capable of predicting the change of the catalytic performance by catalyst mileage. Additionally, Ramanathan et al.[9] employed different vehicle data sets to estimate the kinetic parameters of a TWC global kinetic model. The model was able to predict the light-off temperature of new data sets reasonably well.

New emission regulations have not only introduced more rigorous limits for gaseous pollutants but also for particle emissions. The latest European emission regulations are set on the basis of both mass and number counts to guarantee the reduction of the ultrafine particles.[10] The PM and PN European regulation (Euro 6c) are set at 4.5 mg/km and 6
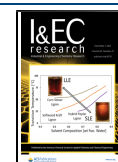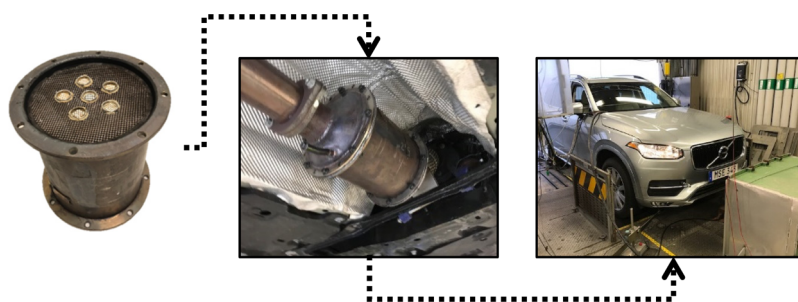
Figure 1. Real soot collection procedure based on 10 h running aggressive RDE cycles in the vehicle chassis dynamometer. The injection timing and lambda set-point were modified to accelerate the soot collection.

$\times$ 10^{11} #/km, on the World-Harmonized Light-duty Test Cycle, WLTC.[11−13] In addition, particle number regulations of 9 × 10^{11} #/km should also be followed under real driving conditions (Euro 6d-TEMP).[11] PM regulations in US (California LEVIII and US Tier 3) require vehicles to emit less than 3 mg/mi by 2021 and further down to 1 mg/mi in California from 2025.[14,15] Meanwhile, China is following the European framework with some variations.[11]

Therefore, in order to comply with current and future PM/PN limits, it is very likely that car manufacturers will equip gasoline-powered vehicles with gasoline particulate filters (GPFs). It is likely that the most economical way to use this technology in a gasoline exhaust system is by combining TWC + GPF in one single device (referred to as a catalyzed gasoline particulate filter (cGPF), or four-way catalyst).[16,17] This technology consists of a TWC catalytic material impregnated on the porous walls of the particle filter. This system configuration may bring potential benefits in terms of vehicle system configuration and overall cost.[13] For vehicles with very little ground clearance, the filter must be mounted in a location close to the engine.[14] This technology can be also mounted in the underbody position, downstream of the TWC(s). In this case, the system will be colder and will tend to trap more soot.[14] Some research work has already been done for cGPF technology, and it is expected to be adopted extensively in the future.[12,13,16−20] However, cGPFs need to take into account both the effect of soot and ash loading. It is well documented that the TWC functionality of cGPFs is affected in the presence of ash.[13,17,20] In an earlier publication,[21] the catalytic performance of soot-free and soot-loaded samples was compared under different feed temperatures and feed gas mixtures. It was demonstrated that the soot accumulation on cGPFs has a large effect on the gaseous pollutant conversion due to the deposition of soot onto their active sites. This soot inhibition effect, which is negligible in TWC converters because of their inherent low filtering efficiency, is simulated in the present study with a global kinetic model.

The objective of this article is to understand the relevant TWC reaction mechanisms and kinetic processes taking place both in clean and soot-loaded filters. The model captures most of the experimental trends reported in the previous publication, particularly when using a Pd/CeZr/Al$_2$O$_3$-coated GPF converter.

2. EXPERIMENTAL PROCEDURE

2.1. Catalyst Preparation. The preparation of the CeZrO$_2$/γ-Al$_2$O$_3$ catalyst support was done by a citrate complexation incipient wetness impregnation method,[22−24] details of which can be found in our earlier publication.[21]

Thereafter, 0.92 wt % palladium was then added to the support CeZrO$_2$/γ-Al$_2$O$_3$ using the incipient wetness impregnation method. The Pd(NO$_3$)$_2$ (Heraeus GmbH, 16.37 wt % Pd, Hanau, Germany) precursor was first dissolved in deionized water and impregnated on to the support. The material was dried at 110 °C and calcined at 550 °C for 2 h. Pd/CeZr/Al$_2$O$_3$ was washcoated onto a commercial GPF substrate intended for coating. The substrate was 300 cpsi, with a wall thickness of 8 mil. The dimension was 13 mm in diameter and 20 mm in length, with a washcoat loading of 270 mg.

2.2. Soot Collection. Before collecting the soot, the monolith was treated for 20 h at 650 °C in 5% H$_2$O and 10% O$_2$, using a total flow of 3 L/min with Ar balance at atmospheric pressure. After this, every second channel of the monolith was plugged at each end using a slurry (95 wt % θ-Al$_2$O$_3$ and 5 wt % binder (boehmite Disperal P2, Sasol, Brunsbüttel, Germany)). The monoliths were thereafter dried and calcined at 550 °C for 2 h. The monolith was then fitted into a modified commercial GPF converter, as shown in Figure 1, and installed in the underbody of a gasoline Volvo Cars vehicle. Aggressive RDE cycles were run on the vehicle chassis dynamometer for 10 h to collect real soot. The aggressive RDE cycle is often denoted as the RTS95 cycle, which was developed based on the WLTP database with high representation of high load and high speed engine operating points. Note that the lambda set-point and injection timing were changed to increase the soot amount, to facilitate the collection of soot. The amount of soot loaded can be estimated based on CO$_2$ production when oxidizing the soot, which can be found in our previous publication.[21]

2.3. Catalyst Characterization. Transmission electron microscopy (TEM) analysis was conducted to determine the average Pd particle size. After the flow-reactor tests, part of the catalyst powder was scraped off from the monolith for TEM analysis. The catalyst powder was ground in an agate mortar and then placed on a carbon film employing TEM Cu grids. Samples were imaged using an FEI Titan 80−300 TEM. The images were collected using a high-angle annular dark field detector in the scanning TEM (STEM) imaging mode. Energy-dispersive spectroscopy was also employed to determine the presence of precious metals. Particle size analysis was performed with ImageJ.

The measurement of the specific surface area was also performed by using the nitrogen physisorption method at −196 °C on a Micromeritics TriStar 3000 instrument. Half of the sample monolith was crushed and pretreated in a vacuum at 225 °C for 2 h. The specific surface area was obtained from the linear part of the Brunauer-Emmett-Teller (BET) curve. Moreover, the specific surface area of the substrate was

measured and subtracted from the measured BET curve of the real samples.

Additionally, the coated GPF sample was studied in sections using elemental mappings by scanning electron microscopy and energy-dispersive X-ray (SEM−EDX). The experiment was performed in low-vacuum mode using an FEI Quanta 200 ESEM equipped with an Oxford Inca EDX.

2.4. Flow-Reactor Experiments. The catalytic activity of the sample was tested in a continuous gas flow reactor, which consisted of a horizontal quartz tube with heating and insulation. The monolith was wrapped in an inert expandable mat to hinder bypass of the gas flow. The temperature was measured using two K-type thermocouples. One thermocouple was placed 10 mm upstream the monolith to measure the temperature of the gas phase, while the second was located in the rear part of the monolith to monitor the reaction temperature. The total flow rate was kept constant at 4000 mL/min throughout the course of each experiment by use of Ar balance. The inlet gas composition was controlled by separate mass flow controllers (Bronkhorst), while the reactor outlet composition was measured with a calibrated FTIR spectrometer (MKS 2030 HS).

Prior to testing, a pretreatment procedure was carried out at 550 °C for 1 h in the presence of Ar. Then, the catalytic activity of the soot-free sample was tested under steady-state conditions from 200 to 500 °C in the presence of different reductants: carbon monoxide (1% CO), ethene (0.17% C_2H_4), and toluene (560 ppm C_7H_8). The feed gas mixture was composed of CO/hydrocarbon, O_2 (adjustable), CO_2 (12%), and H_2O (5%). The O_2 concentration was adjusted during the experiment to achieve different λ-values, ranging from 0.85 to 1.15, as presented in Figure 2. Note that lambda (λ)
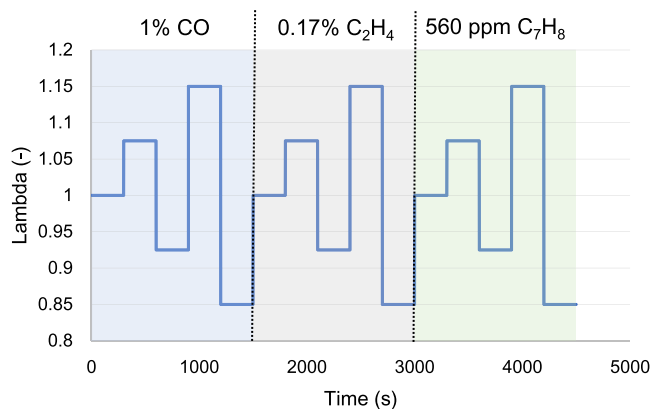

Figure 2. Inlet gas composition at constant temperature using carbon monoxide (1% CO), ethene (0.17% C_2H_4), or toluene (560 ppm C_7H_8) in the presence of O_2 (adjustable), CO_2 (12%), and H_2O (5%).

corresponds to the ratio between the existing oxygen and the oxygen that is required to reach full conversion. Thereafter, the soot-loaded sample was tested following the same procedure described above, except that in this case, the reactor temperature was limited between 125 and 300 °C to prevent soot being burned off. Further information regarding the soot oxidation profile is shown in our earlier publication.[21]

3. MODEL DEVELOPMENT

3.1. Reactor Model. The kinetic model of a TWC-coated GPF was developed in the simulation framework of AVL BOOST aftertreatment. The filter geometry is reduced to one single 1D pair of inlet and outlet channels that are connected by a porous wall. For simplicity, the soot accumulated on the filter is assumed to be located on the filter wall with no soot penetration into the wall. Radial mass transfer from the inlet channel through the wall into the outlet channel is considered in the filter model. The species mass balance equations in the inlet (1) and outlet (2) channels are given by[25]

$$\frac{\partial(m_{gi}\, w_{gi,j})}{\partial t} = -\frac{\partial(\dot{m}_{gi}\, w_{gi,j})}{\partial z}dz - \dot{m}_{gis}w_{gis,j}$$
$$- \rho_{gis}A_{gis}\beta_{gis}(w_{gi,j} - w_{gis,j}) \quad (1)$$

$$\frac{\partial(m_{go}\, w_{go,j})}{\partial t} = -\frac{\partial(\dot{m}_{go}\, w_{go,j})}{\partial z}dz + \dot{m}_{gon}w_{gon,j}$$
$$- \rho_{gon}A_{gon}\beta_{gon}(w_{go,j} - w_{gon,j}) \quad (2)$$

where the time derivative of the inlet and outlet channel masses (m_{gi} and m_{go}) balances the spatial z (axial direction along the channels) derivative of the mass fluxes ($\dot{m}_{gi}$ and $\dot{m}_{go}$), reduced or augmented by two additional wall flow source terms. The first term (second on the right side) is associated with the advective species transfer between channels and walls, whereas the third term on the right side is attributed to the species transfer following the film model. The variables $w_{gi,\,j}$ and $w_{go,\,j}$ represent the mass fraction of species j in the inlet and outlet channels, whereas $w_{gis,\,j}$ and $w_{gon,\,j}$ are the mass fraction of species j from the inlet channel into the wall and from the wall into the outlet channel, respectively. The gas density is denoted by ρ_{gis} at the inlet channel−substrate interface and ρ_{gon} at the outlet channel−substrate interface. A_{gis} and A_{gon} represent the wall surface area in the inlet and outlet channels. Also, β is the mass transfer coefficient of the individual species calculated according to

$$\beta_j = \frac{Sh \times D_j}{d_{hyd}} \quad (3)$$

where Sh is the Sherwood number for fully developed laminar flows in a circular channel ($Sh = 3.657$),[26] D_j is the diffusion coefficient, and d_{hyd} represents the hydraulic diameter of the channel.

Moreover, the gas species balance in the porous wall is given by[25]

$$\frac{\partial(m_{gw}\, w_{gw,j})}{\partial t} = -\frac{\partial(\dot{m}_{gw}\, w_{gw,j})}{\partial x}dx + D_w\frac{\partial}{\partial x}\left(A_w\, \rho_w\, \frac{dw_{gw,j}}{dx}\right)dx$$
$$+ A_w dx\, MG_j \sum v_{w,i,j}\dot{r}_{w,i}(y_j,\, T_s,\, \theta_j) \quad (4)$$

where the time derivative of the wall mass (m_{gw}) balances the spatial x derivative (along the porous filter wall structure) of the mass fluxes ($\dot{m}_{gw}$), changed by additional diffusive (according to Fick's law) and surface storage and reaction terms. MG_j corresponds to the molar mass of species j, and $\dot{r}_{w,\,i}$ is the specific molar reaction rate at the wall multiplied by the stoichiometric coefficient $v_{w,\,i,\,j}$.

The reaction heat was simulated using heat balances built into AVL BOOST software. The energy balance in the gas phase is

$$\varepsilon_g \frac{\partial}{\partial t}\left(\rho_g \sum_k^K \omega_{k,g} h_k\right)$$

$$= -\varepsilon_g \frac{\partial}{\partial z}\left(\rho_g \sum_k^K \omega_{k,g} h_k v_g\right) + \varepsilon_g \frac{\partial}{\partial z}\left(\lambda_g \frac{\partial T_g}{\partial z}\right)$$

$$+ \sum_k^K \varepsilon_g \frac{\partial}{\partial z}\left(\rho_g D_{eff} \frac{\partial \omega_{k,g}}{\partial z} h_k\right) + GSA\, k_h(T_s - T_g)$$

$$(5)$$

where ε_g is the volume fraction of the gas phase, T_g is the gas-phase temperature, h_k is the total enthalpy of component k, λ_g is the thermal conductivity of the gas phase, k_h is the heat transfer coefficient, and GSA is the total channel surface area per unit of substrate volume.

The solid-phase energy balance equation is shown in eq 6

$$(1 - \varepsilon_g)\rho_s \frac{\partial(c_{p,s} T_s)}{\partial t}$$

$$= (1 - \varepsilon_g)\frac{\partial}{\partial z}\left(\lambda_s \frac{\partial T_s}{\partial z}\right) - GSA\, k_h(T_s - T_g)$$

$$+ \sum_i^I \Delta h_i\, r_i(c_k^L, T_s)$$

$$(6)$$

where ρ_s is the density of the solid phase, λ_s is the thermal conductivity of the solid phase, and Δh_i is the heat of reaction.

3.2. Kinetic Model.
This work is a continuation of an earlier publication, where the conversion and durability of model cGPF catalysts were examined experimentally for different temperatures and gas compositions.[21] Based on these experimental results, a global kinetic model was then developed in the current work to capture the CO, C_2H_4, and C_7H_8 conversion behavior both in soot-free and soot-loaded cGPFs. All reaction mechanisms of this kinetic model are described below and summarized in Tables 1−5. Note that the

Table 1. Reactions and Rate Expressions for CO Oxidation and Water-Gas Shift Reactions

	reaction	kinetic rate expression
(R1)	$CO + O_2 \rightarrow CO_2$	$r_1 = \dfrac{Pd_{site}k_1 y_{CO} y_{O_2}}{(1 + K_1^{inh} y_{CO})^2}$
(R2)	$CO + H_2O \rightleftharpoons CO_2 + H_2$	$r_2 = Pd_{site}k_{2f}\left(y_{CO}y_{H_2O} - \dfrac{y_{H_2}y_{CO}}{K_{eq_2}}\right)$

total reaction rates are expressed in kmol/s/m³ (filter volume). These expressions consider the number of active sites taking place in the reaction, which depends on the active metal loading level and dispersion. Likewise, the Arrhenius equation was used in this study to calculate the rate constants (k) according to

$$k_i = A_i e^{-E_{A_i}/RT_s}$$

where A_i is the pre-exponential factor, E_{Ai} the activation energy (J mol⁻¹), R the gas constant (8.314 J mol⁻¹ K⁻¹), and T_s the substrate temperature (K).

3.2.1. CO Abatement Reactions.
CO abatement processes, such as CO oxidation (preferential reaction) and water-gas shift (WGS) reaction, are simulated in this work. First, the rate of CO oxidation was modeled using a Langmuir−Hinshelwood rate expression previously presented by Etheridge and Watling[27] (see Table 1 R1). In this expression, Pd_{site} is the site density, k_1 is the rate constant, y_{CO} and y_{O2} are the mole fractions of CO and O_2, respectively, and K_1^{inh} is the inhibition term, which takes into account the inhibition effect of CO adsorption on the overall reaction rate. K_1^{inh} has no influence on the reaction rate at low concentrations of CO ($K_1^{inh} y_{CO} \ll$ 1), and thus, under such conditions, the CO oxidation rate is first order with respect to both O_2 and CO concentrations. As the CO concentration increases, the K_1^{inh} term becomes important ($K_1^{inh} y_{CO} \gg 1$), resulting in shifting the kinetic order of CO oxidation from positive to negative first order with respect to the CO concentration. It is important to mention that the CO oxidation rate expression used in this work is similar to the classical kinetic equation presented by Voltz et al.[2] in 1973. However, K_1^{inh} is here considered constant, whereas Voltz et al. expressed K_1^{inh} as being dependent on the catalyst temperature. Hlaváček and Votruba[28] also reported K_1^{inh} as a constant. Indeed, the temperature dependencies reported in the literature are generally low, below 10 kJ mol⁻¹, which indicates that it likely is not necessary to make K_1^{inh} temperature dependent.[27,29]

The WGS rate expression (R2) is also presented in Table 1. WGS is an equilibrium reaction, and the equilibrium constant K_{eq2} was determined according to

$$K_{eq_2} = e^{-\Delta G^\ominus / RT_s}$$

where $\Delta G^\ominus$ is the change in standard Gibbs free energy of the system that occurs during the reaction. It is calculated according to

$$\Delta G^\ominus = \Delta H^\ominus - T_s \Delta S^\ominus$$

The enthalpy and entropy changes were determined using the values of standard enthalpy and standard entropy:

$$H - H_{298.15} = At + Bt^2 + \frac{Ct^3}{3} + \frac{Dt^4}{4} - \frac{E}{t} + F - H$$

$$S = A\ln(t) + Bt + \frac{Ct^2}{2} + \frac{Dt^3}{3} - \frac{E}{2t^2} + G$$

where $t = T_s/1000$, and the coefficients were taken from the open NIST Chemistry WebBook.[30]

3.2.2. C_2H_4 Abatement Reactions.
The kinetic rate expression for ethylene is drastically different from the classical Langmuir−Hinshelwood structured rate equation. The rate of reaction varies with the O_2/HC ratio and reaction temperature. Figure 3 shows the ethylene light-off curves as a function of the feed temperature using different lambda conditions from 0.85 to 1.15. At low temperatures (below 225 °C), the light-off showed a nearly similar conversion profile when the oxygen feed concentration was varied. This is indeed characteristic of a zero-order reaction with respect to O_2 and first-order reaction with respect to C_2H_4.[31] As the feed temperature increases (above 225 °C), the light-off curves separate such that higher O_2 feed concentrations lead to lower conversions. This is because ethylene adsorbs more weakly than oxygen on Pd sites, which results in oxygen being the most abundant species on the catalyst surface.[32] This inhibition effect on C_2H_4
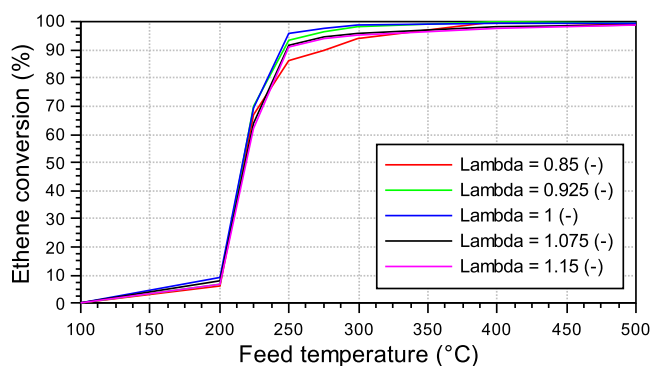
Figure 3. Ethylene conversion as a function of the feed temperature under different lambda conditions.

conversion increases, as the feed becomes leaner. Ethylene indeed reaches full conversion only for slightly rich mixtures (λ = 0.925), since oxygen is removed from the catalyst surface. As oxygen is removed further, C_2H_4 conversion decreases, since there is not enough O_2 to enable the complete oxidation. Therefore, at high temperatures, the oxidation kinetics appear to vary with the O_2/HC ratio. The reaction order switches from positive to negative with respect to oxygen, as the feed becomes leaner; i.e., as the oxygen concentration (lambda) is increased, conversion initially increases but then decreases. In contrast, the oxidation kinetics appear to be zero order with respect to C_2H_4 independent of the feed concentration at feed temperatures above 225 °C.

Based on the above discussion, a kinetic rate expression for C_2H_4 oxidation has been proposed in this work. This expression is presented in Table 2 − R3. A similar rate

Table 2. Reactions and Rate Expressions for C_2H_4 Oxidation and Steam Reforming Reactions

	reaction	kinetic rate expression
(R3)	$C_2H_4 + 3O_2 \rightarrow 2CO_2 + 2H_2O$	$r_3 = \dfrac{Pd_{site}\frac{k_3}{(1+K_3^{inh}y_{O_2})^2}y_{C_2H_4}y_{O_2}}{1 + k_{3C_2H_4}y_{C_2H_4} + \frac{k_{3O_2}y_{O_2}}{(1+K_3^{inh}y_{O_2})^2}}$
(R4)	$C_2H_4 + 2H_2O \rightleftharpoons 2CO + 4H_2$	$r_4 = \dfrac{Pd_{site}k_{4f}\left(y_{C_2H_4}y_{H_2O}^2 - \frac{y_{CO}^2y_{H_2}^4}{K_{eq_4}}\right)}{(1+K_4^{inh}y_{O_2})^3}$

expression was also proposed by Lang et al.[32] This reaction rate expression can be written as

$$r_3 = \frac{Pd_{site}k_{3C_2H_4}\frac{k_{3O_2}}{(1+K_3^{inh}y_{O_2})^2}y_{C_2H_4}y_{O_2}}{1 + k_{3C_2H_4}y_{C_2H_4} + \frac{k_{3O_2}y_{O_2}}{(1+K_3^{inh}y_{O_2})^2}}$$

where the rate constants, k_{3C2H4} and k_{3O2}, can be combined into a single rate constant k_3. At low temperatures, $\frac{k_{3O_2}y_{O_2}}{(1+K_3^{inh}y_{O_2})^2} \gg 1 + k_{3C_2H_4}y_{C_2H_4}$, R3 therefore becomes

$$r_3 = Pd_{site}k_{3C_2H_4}y_{C_2H_4}$$

whereas, at high temperatures, $k_{3C_2H_4}y_{C_2H_4} \gg 1 + \frac{k_{3O_2}y_{O_2}}{(1+K_3^{inh}y_{O_2})^2}$, then R3 is

$$r_3 = Pd_{site}\frac{k_{3O_2}y_{O_2}}{(1+K_3^{inh}y_{O_2})^2}$$

Under this regime (at high temperatures), if $K_3^{inh}y_{O_2} \gg 1$ (lean conditions), the expression becomes

$$r_3 = Pd_{site}\frac{k_{3O_2}}{(K_3^{inh})^2}\frac{1}{y_{O_2}}$$

It is important to mention that K_3^{inh} is defined in this work as being temperature dependent following the Arrhenius equation. In contrast, if $K_3^{inh}y_{O_2} \ll 1$ (rich conditions), the expression becomes

$$r_3 = Pd_{site}k_{3O_2}y_{O_2}$$

The exquisite sensitivity of ethylene to λ at high temperatures also arises from the competition between oxidation and steam reforming (SR) reactions. Similar to the WGS reaction, SR is an equilibrium reaction presented in Table 2 − R4. According to the experimental results, negligible net CO levels were detected under lean experimental conditions, indicating that the SR reaction is completely inhibited by high concentrations of oxygen. This is probably because active site pairs generated by H_2O activation (*,*O) are extinguished under O_2 excess conditions.[33] Oxygen will particularly serve to form less active pairs (*O,*O), which results in an apparent inhibition of the SR reaction.[33] This observation has been well expressed in the reaction rate of this work by introducing an inhibition term in the denominator, which depends on the O_2 concentration.

3.2.3. C_7H_8 Abatement Reactions. The reaction rate expressions for toluene are presented in Table 3, which

Table 3. Reactions and Rate Expressions for C_7H_8 Oxidation and Steam Reforming Reactions

	reaction	kinetic rate expression
(R5)	$C_7H_8 + 9O_2 \rightarrow 7CO_2 + 4H_2O$	$r_5 = \dfrac{Pd_{site}k_5y_{C_7H_8}y_{O_2}}{(1+K_5^{inh}y_{C_7H_8})^2}$
(R6)	$C_7H_8 + 7H_2O \rightleftharpoons 7CO + 11H_2$	$r_6 = \dfrac{Pd_{site}k_{6f}\left(y_{C_7H_8}y_{H_2O}^7 - \frac{y_{CO}^7y_{H_2}^{11}}{K_{eq_6}}\right)}{1 + K_6^{inh}y_{O_2}}$

involves the C_7H_8 oxidation (R5) and steam reforming (R6) reactions. First, the C_7H_8 oxidation expression was taken in accordance with the Langmuir−Hinshelwood structured rate equation, where y_{O_2} and y_{C7H8} are the mole fractions of oxygen and toluene, respectively, and k_5 is the rate constant of the forward reaction. The term $(1 + K_5^{inh}y_{C7H8})^2$ accounts for the inhibition effect by the chemisorption of C_7H_8, where K_5^{inh} represents the inhibition factor. On the other hand, the SR reaction of toluene is an equilibrium reaction with the equilibrium constant K_{eq6}. As with ethylene, this reaction is inhibited under lean conditions, and thus, an inhibition term $(1 + K_6^{inh}y_{O_2})$ dependent on the O_2 concentration was introduced in the denominator of the equation.

3.2.4. Oxygen Storage Reactions. Considering the complicated formulation of a TWC catalyst and strong interactions among ceria, zirconia, and palladium site elements, it is challenging to distinguish the contribution of each of them

to the overall oxygen storage. Moreover, it was found by Yao[34] that the amount of oxygen stored on precious metals is much smaller compared to that on ceria. Thus, the oxygen storage on precious metals and ceria sites was combined together in this work. Table 4 R7 shows the reaction rate expression for the

Table 4. Ceria Reactions and Rate Expressions

	reaction	kinetic rate expression
(R7)	$Ce_2O_3 + 0.5O_2 \rightarrow 2CeO_2$	$r_7 = Ce_{site}k_7y_{O2}(1 - \theta)$
(R8)	$CO + 2CeO_2 \rightarrow Ce_2O_3 + CO_2$	$r_8 = Ce_{site}k_8y_{CO}\theta$
(R9)	$H_2 + 2CeO_2 \rightarrow Ce_2O_3 + H_2O$	$r_9 = Ce_{site}k_9y_{H2}\theta$

oxygen storage. The coverage parameter, θ, is defined as the ratio between the oxygen storage component in the higher oxidation state (more stable) and the total occupied oxygen storage sites, as presented below:

$$\theta = \frac{\text{moles of CeO}_2}{\text{moles of CeO}_2 + 2 \text{ moles of Ce}_2O_3}$$

During rich operation, H_2 and CO are the most reactive species to deplete the stored O_2.[35] Thus, kinetics of oxygen storage capacity depletion by H_2 and CO must be considered in our model. These expressions are also presented in Table 4 (reactions R8 and R9). It should be mentioned that R8 and R9 reactions are usually reversible. Since the reverse reaction rates generally become important at temperatures above 500 °C,[35] we have neglected the reverse reaction in the present work.

3.2.5. Hydrogen Oxidation. Hydrogen produced in the WGS and SR reactions can be also oxidized into H_2O. It was assumed that the surface reaction of adsorbed H_2 and adsorbed O takes place on palladium sites. This assumption is consistent with earlier publication that H_2 oxidation proceeds on the metallic sites.[36] The kinetic rate expression used is presented in Table 5 (R10).

Table 5. H_2 Oxidation Reaction and Rate Expression

	reaction	kinetic rate expression
(R10)	$H_2 + 0.5O_2 \rightarrow H_2O$	$r_{10} = Pd_{site}k_{10}y_{H2}y_{O2}$

4. RESULTS AND DISCUSSION

4.1. Catalyst Characterization. The average Pd particle size was calculated from STEM images, as presented in Figure 4. The average Pd particle size was 24.7 nm, which resulted from the measurement of 57 different particles. The calculation was performed assuming that the precious metals had spherical shapes and were equally distributed over the support, using the following formula:

$$d_D = 2\sqrt{\frac{A_p}{\pi}}$$

A_p represents the area of the particle, and d_D is the particle diameter. Based on the particle size, the precious metal dispersion was derived using the following relation:[37]

$$D = \frac{1.11}{d_D}$$

where D is the precious metal dispersion ($0 < D < 1$) and d_D is given in nanometers. This calculation resulted in a dispersion of 4.5%. Moreover, the specific surface area from the BET measurements resulted in 90.4 m^2/g.

Furthermore, the coated GPF sample was divided into sections, and the cross-sectioned areas of the filter walls were examined by SEM–EDX, as presented in Figure 5. Support elements of aluminum, cerium, and zirconium appeared to penetrate deep into the filter wall with a homogeneous distribution over the whole porous substrate material. This means that the entire monolith is catalytically active, and reactions are not restricted to certain regions within the geometry. Note that the filter substrate also contains Al.

4.2. Kinetic Parameter Estimation with the Clean Filter. Figure 6 shows the experimental and simulated outlet concentrations of CO, C_2H_4, and C_7H_8 for the soot-free catalyst under different feed temperatures and lambda conditions. A magnification of the outlet concentrations of C_2H_4 with a soot-free catalyst under different feed temperatures and lambda conditions is presented in Figure S1 in the Supporting Information (SI). Note that the conversion efficiencies of CO, C_2H_4, and C_7H_8 with soot-free and soot-loaded samples are shown in our previous publication.[21] The kinetic parameters for the model are given in Table 6 and the
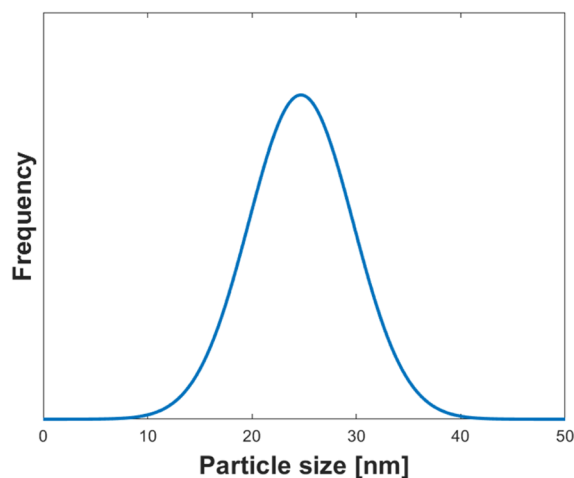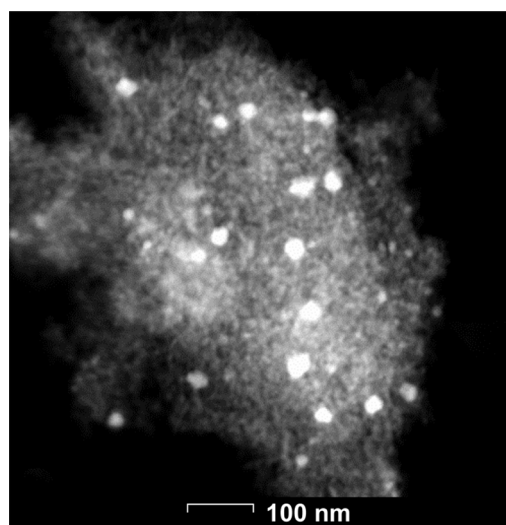

Figure 4. STEM image (left) and the particle size distribution (right) determined from the measurement of 57 Pd particles.
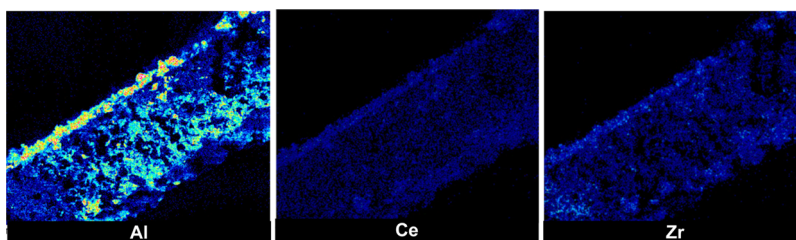
Figure 5. SEM−EDX mapping of the catalyst distribution within the filter wall.

Figure 6. Outlet concentrations of (A) CO, (B) C_2H_4, and (C) C_7H_8 with a soot-free catalyst under different feed temperatures and lambda conditions. The experimental results are presented with solid blue lines, while the simulation results are shown with solid red lines. The inlet CO/HC concentrations are given in Figure 2. In addition, O_2 (variable), CO_2 (12%), and H_2O (5%) were present.

additional parameters in Table S1 (Supporting Information). The kinetic parameters were initially manually tuned using the

commercial software AVL BOOST. The manual tuning consisted of fitting first the kinetic parameters to the

Table 6. Kinetic Parameters

reaction	enthalpy of reaction (kJ/mol)	pre-exponential factor (s^{-1})	activation energy (kJ/mol)
R1	−283	8×10^{15}	93.0
R2	−41.2	3×10^{12}	85.0
R3	−1323	2.5×10^{24}	163.1
R4	210	3×10^{18}	105.7
R5	−3771.9	2.6×10^{19}	138.9
R6	868.9	6.5×10^{19}	97.3
R7	−100	5×10^{7}	62.0
R8	−183	5×10^{5}	40.0
R9	−142	1×10^{4}	35.0
R10	−242	6.5×10^{15}	90.0

experimental results of the oxidation reactions under lean conditions, since under this regime, WGS and SR reactions were inhibited. Thereafter, WGS and SR parameters were tuned under rich conditions. After the manual tuning, the optimization of the parameters was also carried out with the software AVL Design Explorer using the Genetic Algorithm method.

The model is able to describe adequately the experimental results for all three reductants over a broad range of operating conditions. The estimated kinetic parameters appeared to be in agreement to those presented in the literature. For instance, the activation energy of CO was estimated at 93 kJ/mol for the so-called monofunctional path (reaction on the precious
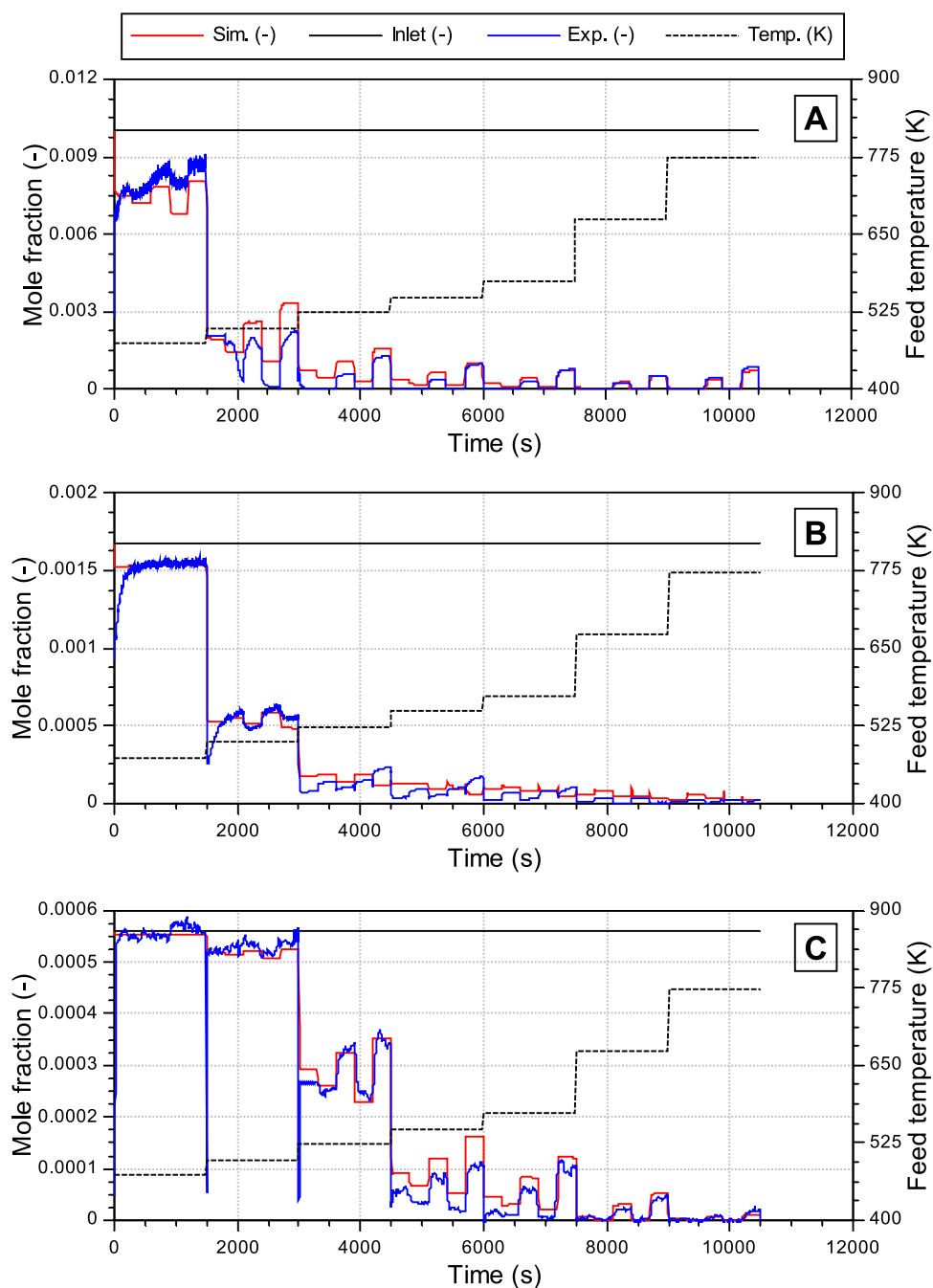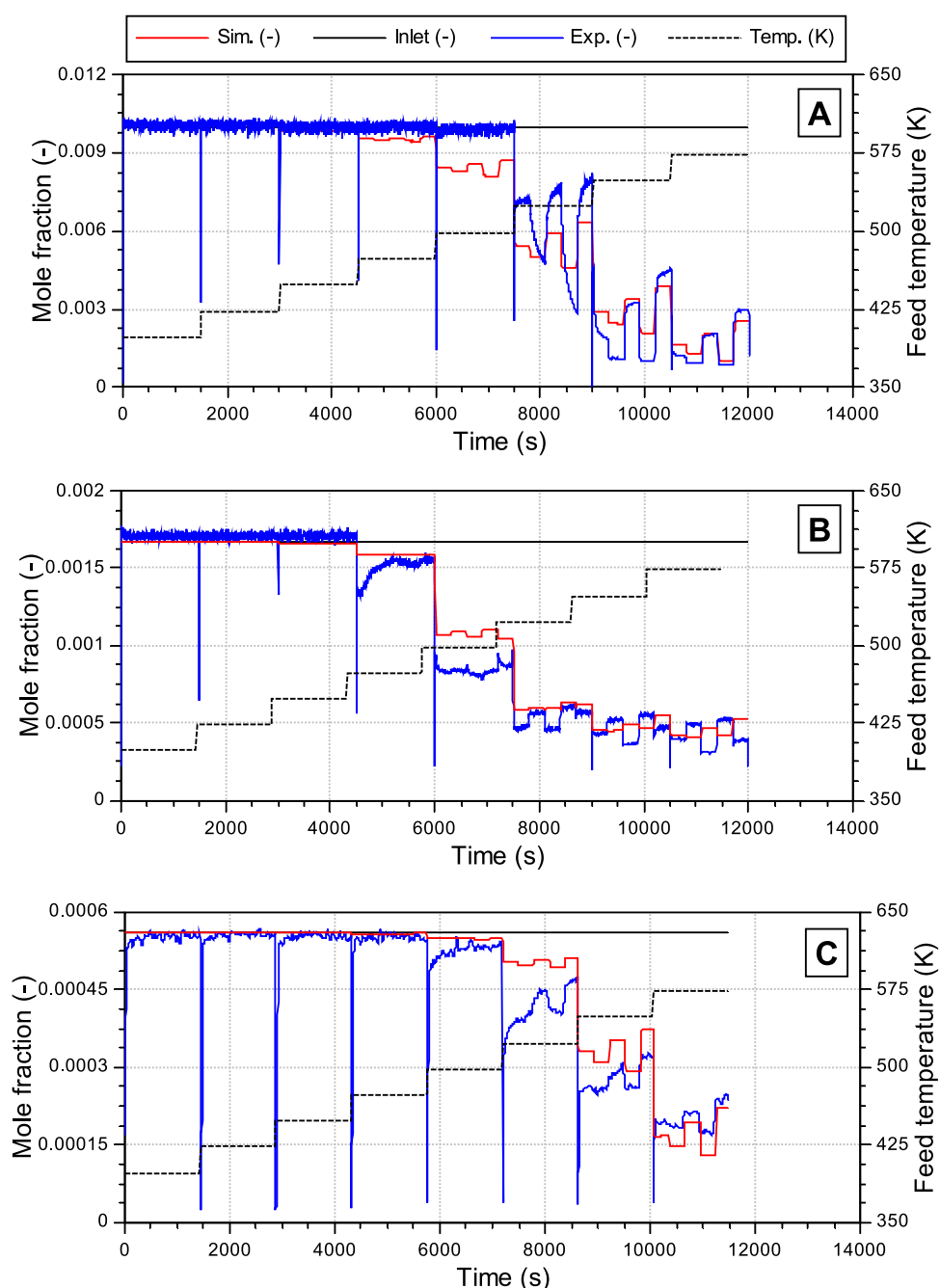

Figure 7. Outlet concentrations of (A) CO, (B) C_2H_4, and (C) C_7H_8 with a soot-loaded catalyst under different feed temperatures and lambda conditions. The experimental results are presented with solid blue lines, while the simulation results are shown with solid red lines.

metals only), while it is presented in the literature in a range from 88 to 122 kJ/mol[1,9,38] for TWC. This activation energy is generally close to the binding energy of absorbed CO.[39] This is because the catalyst surface is almost completely covered by CO under reaction conditions, and hence, the reaction rate is controlled by the rate of CO desorption. Oxygen can only adsorb at precious metal sites where CO has desorbed, resulting in first-order dependence in O_2 and negative first-order dependence in CO, as presented in the reaction expression R1 (see Table 1). Further CO conversion was achieved with the so-called bifunctional path in which the reaction takes place at the noble metal/ceria interface.[40] This path first involves the oxygen adsorption on ceria sites (R7) under O_2 excess conditions, which was estimated with an activation energy of 62 kJ/mol in the present work, in line with some other studies where 67 kJ/mol was found.[41] Thereafter, ceria is reduced by CO and H_2 under conditions of low oxygen concentrations. Both reactions were estimated with activation energies of 40 and 35 kJ/mol. Furthermore, the WGS reaction also contributed to CO conversion. The estimated activation energy of the WGS also agrees with the literature. Shwan et al.[42] reported 76 kJ/mol for an NO_X storage and reduction catalyst, and Han et al.[43] calculated apparent activation energies of 76.7 and 169.8 kJ/mol for a fresh and aged Pd/$Ce_{0.67}Zr_{0.33}O_2$/Al_2O_3 catalyst, similar to the sample synthesized in this study.

The model also predicted the C_2H_4 conversion very well over the broad range of temperatures and feed O_2 concentrations. In particular, the inhibition effect of oxygen was adequately captured by the model under high O_2 feed concentrations. Note that the estimated overall activation energy was high at 163.1 kJ/mol. In fact, studies have reported a wide range of activation energies, between 40 and 200 kJ/mol, mostly depending on the type of ethylene surface species formed.[44−50] There are two types of surface species: π-bonded ethylene, which is oxidized very fast, and di-σ ethylene, which is oxidized much more slowly.[48] π-Bonded ethylene is adsorbed on one single precious metal site, while di-σ ethylene is adsorbed on two active sites (more stable).[48] This is in agreement with the binding energies reported in the literature, where di-σ ethylene is in a range from 131 to 200 kJ/mol,[45−47] while π-bonded ethylene has been assigned from 40 to 54 kJ/mol.[44,51] It is therefore reasonable to assume, based on the high activation energy obtained, that the principal adsorption mode for C_2H_4 in the present work is di-σ ethylene. The formation of di-σ bonding is usually accompanied by the formation of several products, such as ethylidyne and methylidyne groups, vinyl species, etc.[51] The formation of these species depends on the temperature and surface coverage.[51] In addition, SR was also considered for C_2H_4 conversion under rich conditions. The activation energy was estimated to be 105.8 kJ/mol, whereas the inhibition factor was computed based on the Arrhenius equation (A_4^{inh}, E_4^{inh}) defined above.

The kinetic model was also able to describe satisfactorily the experimental results for toluene conversion, as presented in Figure 6C. The activation energies for the oxidation and for the SR reactions were estimated to be 138.9 and 97.3 kJ/mol, respectively. In particular, the toluene oxidation was between 106 kJ/mol calculated by Ordóñez et al.[52] and 161 kJ/mol reported by Morales-Torres et al.[53] for the oxidation of toluene on palladium catalysts supported on carbon nanofibers. Similar to CO oxidation, toluene oxidation is strongly dependent on

O_2 concentration and inhibited by the strong adsorption of the unsaturated hydrocarbon on the Pd surface by π-bonds.[34] This strong interaction of the hydrocarbon with the catalyst surface is explained by the fact that the methyl group in the C_7H_8 structure raises the electronic density of the aromatic ring, making the interaction between the catalyst surface and the molecule stronger.[52] Therefore, at high C_7H_8 concentrations, the catalyst surface is almost completely covered by toluene, and the reaction rate is determined by the surface concentration of oxygen. In contrast, at low toluene concentrations, toluene oxidation is faster and the hydrocarbon surface concentration is the controlling factor.

4.3. Soot Inhibition Effect on TWC Reactions. According to our previously published study,[21] the TWC reactions of cGPFs were affected in the presence of soot. Soot-loaded samples presented lower conversion efficiencies with respect to soot-free cGPFs, indicating that part of the active sites were masked by the accumulation of soot on the filter. This masking effect blocks or limits the access of reactants to the active sites, inhibiting the gaseous pollutant conversion. This is well documented in the literature.[54,55] Thus, this inhibition effect was simulated in this study over the Pd/CeZr/Al_2O_3 sample using the reaction expressions and kinetic parameters estimated above, with the purpose of understanding the kinetic processes taking place in the presence of soot over the whole range of operating conditions. Compared to soot-free experiments, the feed temperature was limited between 125 and 300 °C to prevent the soot oxidation, whereas λ-values were kept the same, ranging from 0.85 to 1.15.

Figure 7 shows the experimental and simulated outlet concentrations of CO, C_2H_4, and C_7H_8 for the soot-loaded catalyst. In this case, the inhibition of soot was simulated through the reduction of palladium and ceria site density (both with the same proportion), according to Table 7. This

Table 7. Site Density Reduction for CO, C_2H_4, and C_7H_8 because of the Soot Inhibition Effect

species	site density reduction (%)
CO	77
C_2H_4	31
C_7H_8	72

reduction in site density was carried out to fit the simulated results to the experimental data. The kinetic parameters estimated with the clean filter were kept constant. These results clearly show that ethylene seems to be less affected by the presence of soot compared to CO and toluene. The latter species presented similar results with a reduction of active site density of around 75%, whereas the reduction was only 31% for C_2H_4. This observation is probably related to the type of surface species formed. As mentioned above, CO and toluene share similar chemisorption behavior with a strong adsorption on a single active site through π-bonds.[34] In contrast, ethylene may adsorb on sites, covered with oxygen, with the primary adsorption mode of di-σ bonding. Di-σ bonding can be initially formed from π-bonded species[48] and can be then also accompanied by the formation of other more stable and less reactive products. This is only possible when a large number of vacant sites are available at the catalyst surface.[48] It is therefore reasonable to assume that the accumulation of soot on the filter reduced the number of active sites on the catalyst surface,
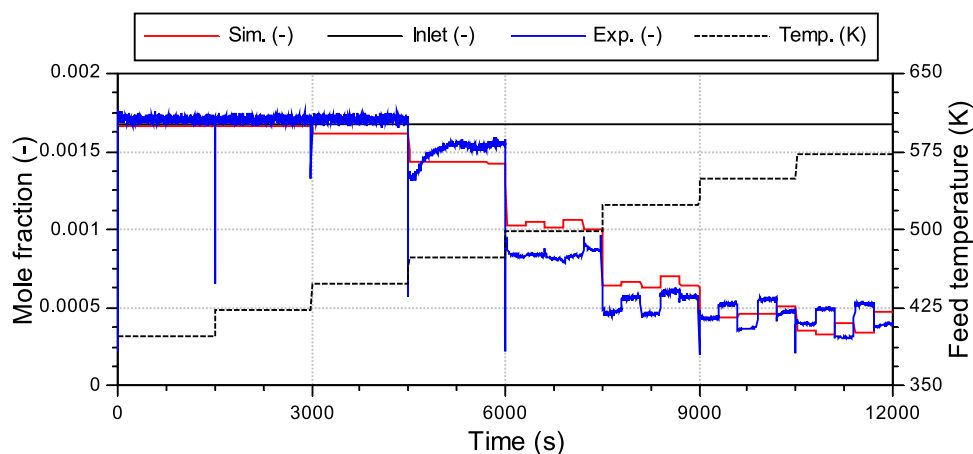
Figure 8. Simulated and experimental outlet concentrations of C_2H_4 for the soot-loaded catalyst under different feed temperatures and lambda conditions. The kinetic parameters have been modified with respect to the soot-free parameters, with a site density reduction of 75%.

inhibiting the formation of more stable C_2H_4 species. Instead, more reactive species, like π-bonded species, were probably formed due to the lack of vacant sites, resulting in a lower soot inhibition effect over C_2H_4 compared to CO and toluene.

This observation therefore indicates that the kinetic parameters of C_2H_4 varied in the presence of soot. Using the same number of active site reductions as with CO and toluene, the kinetic parameters of C_2H_4 oxidation were adjusted to corroborate the formation of more reactive species. Figure 8 shows the simulated and experimental outlet concentrations of C_2H_4 for the soot-loaded catalyst with a site density reduction of 75%, and the adjusted kinetic parameters are given in Table 8. The activation energy of the ethylene oxidation reaction was

Table 8. Kinetic Parameters for C_2H_4 Oxidation for the Soot-Loaded Sample

parameters	value
site density reduction	75%
pre-exponential factor of k_3	3.1×10^{19} (s^{-1})
activation energy of k_3	105,300 (J/mol)
pre-exponential factor of k_{3O2}	7×10^{14} (−)
activation energy of k_{3O2}	300 (J/mol)
pre-exponential factor of k_{3C2H4}	44,000 (−)
activation energy of k_{3C2H4}	105,000 (J/mol)

significantly decreased from 163 to 105 kJ/mol in the presence of soot (see Table 6 and Table 8). This clearly shows the formation of less stable and more reactive species on Pd sites as the number of vacant sites is reduced by the soot masking effect.

5. CONCLUSIONS

A global kinetic model for TWC-coated GPFs was developed in this work to understand the relevant TWC reaction mechanisms and kinetic processes taking place both in clean and soot-loaded filters. Flow-reactor results from our previous publication were here employed to develop reaction rate expressions and to estimate kinetic parameters. The experiments were performed over a model $Pd/CeZr/Al_2O_3$ catalyst hydrothermally treated at 650 °C in which real soot was directly collected from a Volvo gasoline vehicle. Overall, the model is able to describe adequately the experimental results for all three reductants (CO, C_2H_4, and C_7H_8) over the broad

range of feed temperatures and O_2 concentrations. In particular, ethylene presented different oxidation trends compared to CO and toluene. At low temperatures, the reaction order was positive with respect to ethylene and zero order with respect to oxygen, i.e., with no ethylene self-inhibition. At high temperatures, the reaction orders appeared to change to negative order with respect to oxygen and zero order with respect to ethylene. Based on these observations, a kinetic expression for ethylene oxidation was proposed in this work that is able to capture most of the experimental trends observed.

Ethylene also exhibited a different behavior in the presence of soot compared to CO and toluene. The soot inhibition was modeled through the reduction of the active site density based on the fact that the soot accumulation masks the active sites, limiting or blocking the access of reactants. CO and C_7H_8 presented similar site density reduction, while C_2H_4 seemed to be less affected by the presence of soot. This observation may be associated with the formation of less stable and more reactive species on the catalyst surface due to the reduction of vacancies on the catalyst. This effect was corroborated by adjusting the kinetic parameters of C_2H_4 using the same number of active sites as used with CO and toluene, resulting in a substantial reduction of the activation energy required for the ethylene oxidation reaction.

■ ASSOCIATED CONTENT

ⓢ Supporting Information

The Supporting Information is available free of charge at https://pubs.acs.org/doi/10.1021/acs.iecr.1c02742.

Magnification of Figure 6b and additional parameters for the model (PDF)

■ AUTHOR INFORMATION

Corresponding Author

Louise Olsson − *Chemical Engineering, Competence Centre for Catalysis, Chalmers University of Technology, Gothenburg SE-412 96, Sweden;* ⓞ orcid.org/0000-0002-8308-0784; Email: louise.olsson@chalmers.se

Authors

Jesus De Abreu Goes − *Volvo Cars, Gothenburg SE-405 31, Sweden; Chemical Engineering, Competence Centre for*

Catalysis, Chalmers University of Technology, Gothenburg SE-412 96, Sweden

Timothy C. Watling − *Johnson Matthey, Sonning Common, Reading RG4 9NH, U.K.;* ● orcid.org/0000-0003-2050-6183

Complete contact information is available at:
https://pubs.acs.org/10.1021/acs.iecr.1c02742

Notes
The authors declare no competing financial interest.

■ NOMENCLATURE LIST

A_{gis}	wall surface area in the inlet channel (m^2)
A_{gos}	wall surface area in the outlet channel (m^2)
A_w	flow cross section in the wall (m^2)
A_j	pre-exponential factor for reaction i (s^{-1})
Ce_{site}	cerium surface site density (mol/m^3)
d_{hyd}	hydraulic diameter of the channel (m)
D_j	diffusion coefficient for species j
E_{Ai}	activation energy for reaction i (J/mol)
ΔG	Gibbs free energy (J/mol)
ΔH	enthalpy change (J/mol)
K_{eq}	equilibrium constant (−)
k_i	rate constant for reaction i (s^{-1})
m_{gi}	mass of the gas phase in the inlet channel (kg)
m_{go}	mass of the gas phase in the outlet channel (kg)
$\dot{m}_{gis}$	mass flow from the inlet channel into the wall (kg/s)
$\dot{m}_{gon}$	mass flow from the wall into the outlet channel (kg/s)
MG_j	molar mass of gas-phase species j (kg/mol)
Pd_{site}	palladium surface site density (mol/m^3)
$\dot{r}_{w,i}$	reaction rate for reaction i ($mol/s/m^3$ volume of monolith)
R	gas constant (J/(mol K))
ΔS	entropy change (J/(mol K))
Sh	Sherwood number (−)
T_s	temperature at the catalyst surface (K)
t	time (s)
x	spatial coordinate along the porous filter wall structure (m)
$w_{g,j}$	mass fraction of species j (−)
y_j	mole fraction of species j (−)
z	spatial coordinate along the channels (m)

Greek letters

β	mass transfer coefficient (m/s)
ν	stoichiometry coefficient in the filter wall (−)
ρ	density (kg/m^3)
θ_j	coverage parameter (−)
θ	coverage parameter for oxygen storage on ceria (−)

■ REFERENCES

(1) Dubien, C.; Schweich, D.; Mabilon, G.; Martin, B.; Prigent, M. Three-way catalytic converter modelling: fast- and slow-oxidizing hydrocarbons, inhibiting species, and steam-reforming reaction. *Chem. Eng. Sci.* **1998**, *53*, 471−481.

(2) Voltz, S. E.; Morgan, C. R.; Liederman, D.; Jacob, S. M. Kinetic Study of Carbon Monoxide and Propylene Oxidation on Platinum Catalysts. *Product R&D* **1973**, *12*, 294−301.

(3) Subramanian, B.; Varma, A. Reaction kinetics on a commercial three-way catalyst: the carbon monoxide-nitrogen monoxide-oxygen-water system. *Ind. Eng. Chem. Prod. Des. Dev.* **1985**, *24*, 512−516.

(4) Nibbelke, R. H.; Campman, M. A. J.; Hoebink, J. H. B. J.; Marin, G. B. Kinetic Study of the CO Oxidation over Pt/γ-Al₂O₃ and Pt/Rh/CeO₂/γ-Al₂O₃ in the Presence of H₂O and CO₂. *J. Catal.* **1997**, *171*, 358−373.

(5) Nibbelke, R. H.; Nievergeld, A. J. L.; Hoebink, J. H. B. J.; Marin, G. B. Development of a transient kinetic model for the CO oxidation by O₂ over a Pt/Rh/CeO₂/γ-Al₂O₃ three-way catalyst. *Appl Catal B* **1998**, *19*, 245−259.

(6) Hauck, C.; Tischer, S.; Maier, L.; Deutschmann, O. Modelling of local aging effects of commercial three-way catalysts: Spatial temperature and CO conversion profiles. *Can. J. Chem. Eng.* **2014**, *92*, 1587−1596.

(7) Kang, S. B.; Nam, I.-S.; Cho, B. K.; Kim, C. H.; Oh, S. H. Kinetic model for modern double-layered Pd/Rh TWC as a function of metal loadings and mileage. *Chem. Eng. J.* **2015**, *278*, 328−338.

(8) Kang, S. B.; Kwon, H. J.; Nam, I.-S.; Song, Y. I.; Oh, S. H. Activity Function for Describing Alteration of Three-Way Catalyst Performance over Palladium-Only Three-Way Catalysts by Catalyst Mileage. *Ind. Eng. Chem. Res.* **2011**, *50*, 5499−5509.

(9) Ramanathan, K.; Sharma, C. S. Kinetic Parameters Estimation for Three Way Catalyst Modeling. *Ind. Eng. Chem. Res.* **2011**, *50*, 9960−9979.

(10) Guan, B.; Zhan, R.; Lin, H.; Huang, Z. Review of the state-of-the-art of exhaust particulate filter technology in internal combustion engines. *J. Environ. Manage.* **2015**, *154*, 225−258.

(11) Joshi, A.; Johnson, T. V. Gasoline Particulate Filters—a Review. *Emiss. Contr. Sci.Technol.* **2018**, *4*, 219−239.

(12) Shao, H.; Carpentier, G.; Yin, D.; Wang, Y.; Remias, J.; Roos, J.; Xia, W.; Zheng, Y.; Yuan, X.; Yang, D.; He, X.; Yin, Z. *Engine Accelerated Aging Method Developed to Study the Effect of Lubricant Formulations on Catalyzed Gasoline Particulate Filter Durability*; SAE Technical Paper, 2018 2018-01-1804.

(13) Xia, W.; Yuan, X.; Yang, D.; Zheng, Y.; Zhao, D.; Wang, C.; He, X.; Shao, H.; Carpentier, G.; Remias, J.; Roos, J.; Yin, D.; Wang, Y.; Liang, K. J. *Design of Catalyzed Gasoline Particulate Filter (cGPF) and Investigation of Its Durability Performance Using Accelerated Engine Aging*; SAE Technical Paper, 2019 2019-01-0970.

(14) Lambert, C.; Chanko, T.; Dobson, D.; Liu, X.; Pakko, J. Gasoline Particle Filter Development. *Emiss. Contr. Sci. Technol.* **2017**, *3*, 105−111.

(15) Johnson, T.; Joshi, A. Review of Vehicle Engine Efficiency and Emissions. *SAE Int. J. Engines* **2018**, *11*, 1307−1330.

(16) Opitz, B.; Drochner, A.; Vogel, H.; Votsmeier, M. An experimental and simulation study on the cold start behaviour of particulate filters with wall integrated three way catalyst. *Appl Catal B* **2014**, *144*, 203−215.

(17) Mitsouridis, M. A.; Karamitros, D.; Koltsakis, G. Model-Based Analysis of TWC-Coated Filters Performance. *Emiss. Contr. Sci. Technol.* **2019**, *5*, 238−252.

(18) Arunachalam, H.; Pozzato, G.; Hoffman, M. A.; Onori, S. *In Modeling the thermal dynamics inside a ceria-coated Gasoline Particulate Filter*; 2017 IEEE Conference on Control Technology and Applications (CCTA), 2017; 99−105.

(19) Xia, W.; Zheng, Y.; He, X.; Yang, D.; Shao, H.; Remias, J.; Roos, J.; Wang, Y. *Catalyzed Gasoline Particulate Filter (GPF) Performance: Effect of Driving Cycle, Fuel, Catalyst Coating*; SAE International, 2017 2017-01-2366.

(20) Seong, H.; Choi, S.; Lee, S.; Zaluzec, N. J.; Toops, T. J.; Lance, M. J.; Kim, D.; Nguyen, K. Deactivation of Three-Way Catalysts Coated within Gasoline Particulate Filters by Engine-Oil-Derived Chemicals. *Ind. Eng. Chem. Res.* **2019**, *58*, 10724−10736.

(21) De Abreu Goes, J.; Woo, J. W.; Olsson, L. Effects of Feed Gas Composition on Fresh and Aged TWC-Coated GPFs Loaded with Real Soot. *Ind. Eng. Chem. Res.* **2020**, *59*, 10790−10803.

(22) Di Monte, R.; Fornasiero, P.; Kašpar, J.; Graziani, M.; Gatica, J. M.; Bernal, S.; Gómez-Herrero, A. Stabilisation of nanostructured $Ce_{0.2}Zr_{0.8}O_2$ solid solution by impregnation on Al_2O_3: a suitable method for the production of thermally stable oxygen storage/release promoters for three-way catalysts. *Chem. Commun.* **2000**, *21*, 2167−2168.

(23) Kaspar, J.; Fornasiero, P.; Balducci, G.; Di Monte, R.; Hickey, N.; Sergo, V. Effect of ZrO_2 content on textural and structural properties of CeO_2−ZrO_2 solid solutions made by citrate complexation route. *Inorg. Chim. Acta* **2003**, *349*, 217−226.

(24) He, X.; He, J.; Meng, M. Perovskite-Based Lean-Burn NOxTrap Catalysts Without Using Platinum Group Metals: $K/LaCoO_3/Ce_{1−x}Zr_xO_2$. *Catal. Lett.* **2011**, *141*, 1364.

(25) Wurzenberger, J. C.; Triebl, C.; Kutschi, S. *Diffusion Supporting Passive Filter Regeneration- A Modeling Contribution on Coated Filters*; SAE Technical Paper, 2018 2018-01-0957.

(26) Łojewska, J.; Kołodziej, A. Engineering aspects of catalytic converters designs for cleaning of exhaust gases. *In New and Future Developments in Catalysis : Catalysis for Remediation and Environmental Concerns*; edited by Suib, S. L.; Elsevier: Tokio, 2013, 257−279

(27) Etheridge, J. E.; Watling, T. C. Is reactor light-off data sufficiently discriminating between kinetic parameters to be used for developing kinetic models of automotive exhaust aftertreatment catalysts? The effect of hysteresis induced by strong self inhibition. *Chem. Eng. J.* **2015**, *264*, 376−388.

(28) Hlaváček, V.; Votruba, J. Experimental Study of Multiple Steady States in Adiabatic Catalytic Systems. *In Chemical Reaction Engineering—II*; American chemical society, 1975, *133*, 545 −558.

(29) Hlaváček, V. R. H.; Prins, W.; Van Swaaij, W. P. M. Platinum catalyzed oxidation of carbon monoxide as a model reaction in mass transfer measurements. *Chem. Eng. Sci.* **1998**, *53*, 3355−3366.

(30) NIST *Chemistry WebBook*; https://webbook.nist.gov/ (03/2020),

(31) Gerberich, H. Catalytic oxidation I. The oxidation of ethylene over Pd and Pd-Au alloys. *J. Catal.* **1970**, *16*, 204−219.

(32) Lang, W.; Harold, M. P. Rate Inhibition and Enhancement on Ceria-Promoted Pd Monolith Catalysts: Oxidation of Acetylene, Ethylene, and Propylene and Their Mixtures. *Ind. Eng. Chem. Res.* **2019**, *58*, 6350−6363.

(33) Getsoian, A. B.; Theis, J. R.; Lambert, C. K. Sensitivity of Three-Way Catalyst Light-Off Temperature to Air-Fuel Ratio. *Emiss. Contr. Sci.Technol.* **2018**, *4*, 136−142.

(34) Yao, Y. The oxidation of CO and hydrocarbons over noble metal catalysts. *J. Catal.* **1984**, *87*, 152−162.

(35) Gong, J.; Wang, D.; Li, J.; Currier, N.; Yezerets, A. Dynamic oxygen storage modeling in a three-way catalyst for natural gas engines: A dual-site and shrinking-core diffusion approach. *Appl Catal B* **2017**, *203*, 936−945.

(36) Mandapaka, R.; Madras, G. Aluminium and rhodium co-doped ceria for water gas shift reaction and CO oxidation. *Mol. Catal.* **2018**, *451*, 4−12.

(37) Gremminger, A. T.; Pereira De Carvalho, H. W.; Popescu, R.; Grunwaldt, J.-D.; Deutschmann, O. Influence of gas composition on activity and durability of bimetallic $Pd-Pt/Al_2O_3$ catalysts for total oxidation of methane. *Catal. Today* **2015**, *258*, 470−480.

(38) Millet, C.-N.; Benramdhane, S. *A 3WCC Global Kinetic Model: A Calibration Method Using Laboratory Scale and Engine Test Bench Experiments*; SAE Technical Paper, 2008 2008-01-0453.

(39) Berlowitz, P. J.; Peden, C. H. F.; Goodman, D. W. Kinetics of carbon monoxide oxidation on single-crystal palladium, platinum, and iridium. *J. Phys. Chem.* **1988**, *92*, 5213−5221.

(40) Hoebink, J. H. B. J.; Harmsen, J. M. A.; Balenovic, M.; Backx, A. C. P. M.; Schouten, J. C. Automotive Exhaust Gas Conversion: From Elementary Step Kinetics to Prediction of Emission Dynamics. *Top. Catal.* **2001**, *16*, 319−327.

(41) Galdikas, A.; Descorme, C.; Duprez, D.; Dong, F.; Shinjoh, H. Study of the Oxygen Diffusion on Three-Way Catalysts: A Kinetic Model. *Top. Catal.* **2004**, *30/31*, 405−409.

(42) Shwan, S.; Partridge, W.; Choi, J.-S.; Olsson, L. Kinetic Modeling of NOx Storage and Reduction using Spatially Resolved MS Measurements. *Appl Catal B* **2014**, *147*, 1028−1041.

(43) Han, Z.; Wang, J.; Yan, H.; Shen, M.; Wang, J.; Wang, W.; Yang, M. Performance of dynamic oxygen storage capacity, water−gas shift and steam reforming reactions over Pd-only three-way catalysts. *Catal. Today* **2010**, *158*, 481−489.

(44) Tysoe, W.; Nyberg, G.; Lambert, R. Structural, kinetic, and reactive properties of the palladium (111)-ethylene system. *J. Phys. Chem.* **1984**, *88*, 1960−1963.

(45) Mohsin, S. B.; Trenary, M.; Robota, H. J. Identification of ethylene-derived species on alumina-supported rhodium, iridium, palladium and platinum catalysts by infrared spectroscopy. *J. Phys. Chem.* **1991**, *95*, 6657−6661.

(46) Nibbelke, R. H.; Kreijveld, R. J. M.; Hoebink, J. H. B. J.; Marin, G. B. Kinetic Study of the Ethene Oxidation by Oxygen in the Presence of Carbon Dioxide and Steam over $Pt/Rh/CeO_2/\gamma$-Al_2O_3. In *Studies in Surface Science and Catalysis*; Kruse, N.; Frennet, A.; Bastin, J. M., Eds. Elsevier: 1998; Vol. *116*, 389−398.

(47) Yeo, Y. Y.; Stuck, A.; Wartnaby, C. E.; Kose, R.; King, D. A. Microcalorimetric study of ethylene adsorption at 300 K on Pt{100}-hex and Pt{100}-(1×1). *J. Mol. Catal. A: Chem.* **1998**, *131*, 31−38.

(48) Harmsen, J. M. A.; Hoebink, J. H. B. J.; Schouten, J. C., Transient kinetics of ethylene and carbon monoxide oxidation for automotive exhaust gas catalysis: experiments and modelling. In *Studies in Surface Science and Catalysis*, Froment, G. F.; Waugh, K. C., Eds. Elsevier, 1999, *122*, 101−108.

(49) Harmsen, J. M. A.; Hoebink, J. H. B. J.; Schouten, J. C. Transient Kinetic Modeling of the Ethylene and Carbon Monoxide Oxidation over a Commercial Automotive Exhaust Gas Catalyst. *Ind. Eng. Chem. Res.* **2000**, *39*, 599−609.

(50) Hill, J. M.; Shen, J.; Watwe, R. M.; Dumesic, J. A. Microcalorimetric, Infrared Spectroscopic, and DFT Studies of Ethylene Adsorption on Pd and Pd/Sn Catalysts. *Langmuir* **2000**, *16*, 2213−2219.

(51) Vattuone, L.; Yeo, Y. Y.; Kose, R.; King, D. A. Energetics and kinetics of the interaction of acetylene and ethylene with Pd{100} and Ni{100}. *Surf. Sci.* **2000**, *447*, 1−14.

(52) Ordóñez, S.; Bello, L.; Sastre, H.; Rosal, R.; Díeze, F. V. Kinetics of the deep oxidation of benzene, toluene, n-hexane and their binary mixtures over a platinum on γ-alumina catalyst. *Appl Catal B* **2002**, *38*, 139−149.

(53) Morales-Torres, S.; Pérez-Cadenas, A. F.; Kapteijn, F.; Carrasco-Marín, F.; Maldonado-Hódar, F. J.; Moulijn, J. A. Palladium and platinum catalysts supported on carbon nanofiber coated monoliths for low-temperature combustion of BTX. *Appl Catal B* **2009**, *89*, 411−419.

(54) Lopez-Gonzalez, D.; Tsampas, M. N.; Boréave, A.; Retailleau-Mevel, L.; Klotz, M.; Tardivat, C.; Cartoixa, B.; Pajot, K.; Vernoux, P. Mixed Ionic−Electronic Conducting Catalysts for Catalysed Gasoline Particulate Filters. *Top. Catal.* **2015**, *58*, 1242−1255.

(55) Li, B.; Song, C.; Lv, G.; Chen, K.; Cao, X. Impact of Soot on NOx Adsorption over Cu-Modified Hydrotalcite-Derived Lean NOx Trap Catalyst. *Langmuir* **2017**, *33*, 2939−2948.